J. Fluid Mech. (2006), *vol.* 549, *pp.* 99–129.
doi:10.1017/S0022112005007500 Printed in the United Kingdom

Numerical modelling of convection in a reactive porous medium with a mobile mush–liquid interface

By S. L. BUTLER[1], HERBERT E. HUPPERT[2] AND M. GRAE WORSTER[2]

[1]Department of Geological Sciences, University of Saskatchewan, Saskatoon, SK S7K 5E2, Canada

[2]Institute of Theoretical Geophysics, Department of Applied Mathematics and Theoretical Physics, Centre for Mathematical Sciences, Cambridge University, Wilberforce Road, Cambridge, CB3 0WA, UK

(Received 11 June 2004 and in revised form 26 July 2005)

We describe a series of numerical simulations of dissolution-driven convection in a reactive porous medium heated from above. The physical system consists of a porous medium made of the frozen component of a binary mixture that is immersed in a liquid mixture with which it is in thermodynamic equilibrium. Surface heating results in melting of the uppermost material which releases dense solute and drives compositional convection. An interface develops between the upper region, in which the solid matrix has completely melted, and a lower region, in which the frozen solute evolves. The interface descends as melting proceeds. During the numerical simulations, scaled to be similar to previous experiments using potassium nitrate crystals and their saturated aqueous solution (Hallworth, Huppert & Woods, *J. Fluid Mech.* vol. 535, 2004, p. 255), there are three distinct phases: a purely conductive phase; followed by a phase with very brief, intense, compositionally driven convection; followed by a prolonged phase of more sedate compositionally driven convection in which the average kinetic energy is roughly one order of magnitude less than during the intense early phase. The field equations and the numerical methodology are presented in addition to a simple analytical model for the rate of motion of the interface. The analytical model, valid in the limit of very rapid mixing of the solute, is shown to be in good agreement with the numerical results of purely conductive calculations with a large diffusion coefficient. We investigate solutions for various values of the Rayleigh number and quantify the degree of interface motion as a function of this parameter. These simulations may be particularly applicable to problems associated with post-cumulate processes in magma chambers.

1. Introduction

Many interesting fluid dynamical phenomena can occur in porous media when the interstitial fluid consists of a mixture of more than one component and material can be exchanged between the interstitial liquid and the solid matrix through dissolution and precipitation (Huppert 1990; Phillips 1991; Worster 2000). Because the components of the mixture do not generally partition equally during melting and solidification, the concentration of a solute in the liquid, and hence the density of the interstitial fluid, can be strongly affected by these processes and, under certain circumstances, it can become convectively unstable. In this paper, we present a detailed study, using a numerical model, of compositional convection driven in a two-component reactive

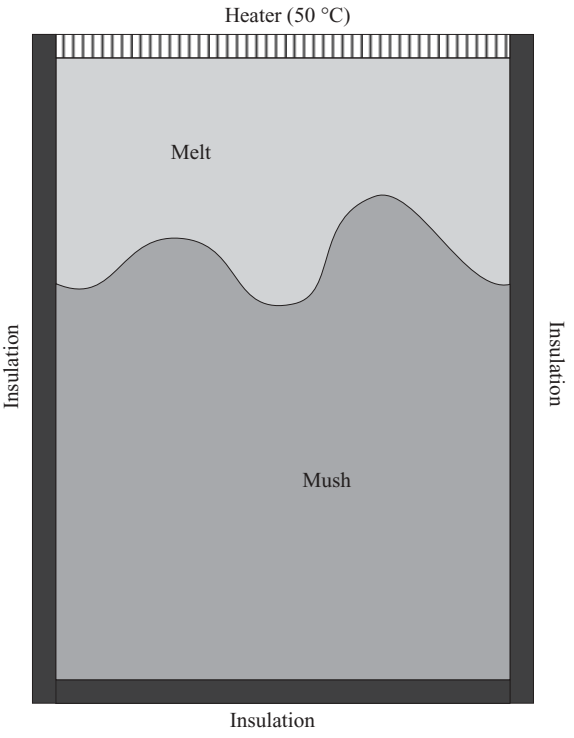

FIGURE 1. A schematic of the system being simulated.

porous medium by heating of the upper surface when the liquid density increases as the result of dissolution of the porous matrix. Of further interest in this system is the formation of a completely molten region in the upper part of the domain and the downward migration of the interface between this region and the remaining porous medium. The rate of displacement of this interface will be studied as a function of the control parameters of the numerical experiments.

Convection in a reactive porous medium can result in significant spatial variations in its porosity. A system of geological interest for which this may be an important process is the crystallization of molten rocks in magma chambers. As discussed in Tait & Jaupart (1992) and Jaupart & Tait (1995), the cooling of magma by contact with country rock may result in the formation of a two-phase region called a mushy layer. A convectively unstable density stratification of the interstitial fluid can occur if the solute concentration of this fluid is altered by internal melting or solidification. Also, a change in solid structure can occur if the interstitial fluid is replaced by a new fluid that is not in equilibrium with the solid matrix and hence causes melting or solidification; the subsequent change in concentration of the fluid can drive convection, a process that may occur in open magma chambers. When the interstitial fluid eventually solidifies there can remain interesting patterns caused by the convection such as the horizontal layering seen in cumulates (Wager & Brown 1968, Irvine 1982).

Aqueous salt solutions have been used for some time as laboratory analogues for geological systems (e.g. Turner & Gustafson 1978; Huppert & Turner 1981; Kerr & Tait 1986; Huppert 1990; Jaupart & Tait 1995; Hallworth, Huppert & Woods 2004). Figure 1 presents a schematic of the physical system modelled here which is scaled to be as similar as possible to laboratory experiments 2a and 2b described in Hallworth

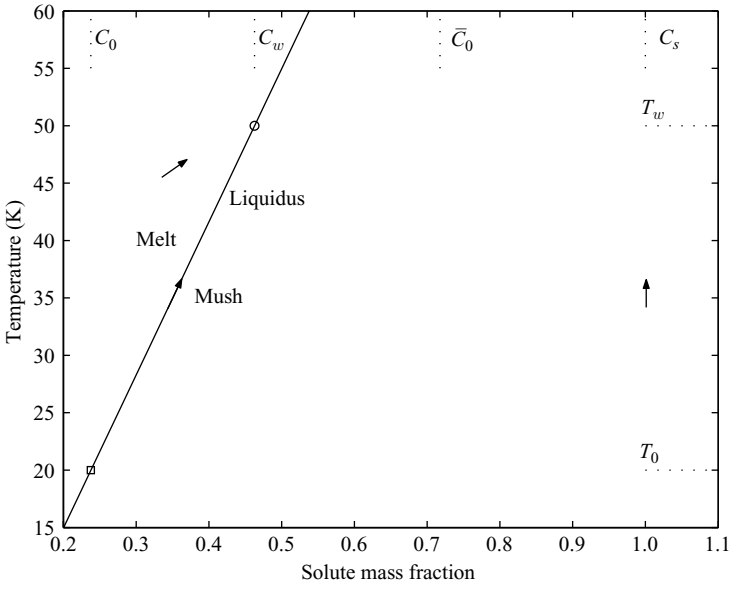

FIGURE 2. The relevant portion of the water–potassium nitrate phase diagram. The solid line is the liquidus and the open square and circle represent the initial and final state of the system. T_0 and T_w are the initial temperature and the imposed temperature of the upper surface while C_0, C_w, $\bar{C}_0$ and C_s are the initial value of the liquid solute concentration, the liquidus concentration at T_w, the initial bulk concentration and the concentration of solute in the solid.

et al. (2004). The domain is initially filled with solid crystals with a spatially uniform porosity immersed in fluid of uniform concentration at its liquidus temperature. The two-dimensional numerical simulation begins when the temperature of the upper boundary is suddenly increased. No material is allowed to enter or leave the domain and all boundaries other than the top are thermally insulating. Heat conducted from the upper surface enters the domain and causes melting of the solid, which results in an upper melt region overlying the remaining mushy layer. One difference between the numerical and laboratory experiments is that, in the simulations, the flow law governing the upper region is that of a porous medium, whereas in the experiments it is that of a free liquid. As we will show, the upper region is stably stratified for most of the simulation, which results in relatively little motion there and hence the effects of the different flow law should be negligible. Although the use of the porous flow law in the upper region is a device to simplify the computation, its effects can be interpreted physically as being caused by a background, inert, fixed, porous medium that takes up a small volume fraction and occupies the entire domain.

Figure 2 presents that part of the phase diagram which is relevant to these simulations. We use the same dimensional concentration and initial and top temperatures as the laboratory experiments of Hallworth *et al.* (2004). The symbols T_w and T_0 represent the imposed temperature of the top surface and the initial temperature of the system, respectively, while C_0, C_w, $\bar{C}_0$ and C_s represent the initial liquid concentration, the liquidus concentration at T_w, the initial bulk concentration (mass of solute in the solid and liquid divided by the total mass of the system) and the concentration of solute in the solid. In our case, we assume that the solid is pure solute ($C_s = 1$), as is appropriate for the aqueous potassium nitrate system used by Hallworth *et al.* (2004). Note also that the eutectic point falls outside of

the parameter range of the simulations and that we are approximating the liquidus by a straight line, as is essentially the case for aqueous potassium nitrate in the appropriate temperature range (Hallworth *et al.* 2004). The square on the diagram indicates the initial state of the spatially uniform system. The arrows lying on the liquidus and pointing vertically on the right-hand side of the diagram indicate the phase trajectories for the interstitial liquid and solid matrix, respectively, in the mushy region while the upper arrow indicates the sense of the trajectory in the melt region. The fluid in the melt region will be warmer than the liquidus temperature. The final temperature of the entire system is known because the system will equilibrate to the surface temperature. The concentration of solute in the fluid depends on whether there is any mush left unmelted once the system has thermally equilibrated. If there is mush remaining, then the final state will be of uniform concentration, C_w. In this case, the fluid concentration in the melt region will converge after a very long time to this value owing to the slow diffusion of solute from the mush. If the mush melts completely, the system will have a uniform concentration equal to the initial bulk concentration. As such, the relative magnitudes of $\bar{C}_0$ and C_w are of crucial importance. If $\bar{C}_0 > C_w$, then there will be mush remaining, while the mush will be completely melted if the opposite is true. The total amount of solid remaining once the system has reached equilibrium can also be predicted from the value of $\bar{C}_0$. What cannot be predicted without a dynamical model is the final height of the interface and the lateral variability of the solid fraction. Understanding these quantities may be important in understanding layered structures mentioned previously that are seen in igneous formations (e.g. Jaupart & Tait 1995; Huppert 2000).

Numerical modelling of reactive porous media is a subject that has received considerable attention in recent years (e.g. Beckermann & Wang 1995). In § 2, we outline the field equations governing flow in a reactive porous medium, while in § 3 we describe our choice of model parameters and initial conditions. In § 4, we outline a novel numerical method for solving the system. We outline in § 5 a simple analytical model that gives insight into the factors controlling the rate of descent of the interface. In § 6, we describe how average quantities in the numerical model vary as a function of time for various values of the porous-medium Rayleigh number while in § 9 we describe in detail the time variation of the various fields characterizing the system for the simulation that was run with the largest Rayleigh number and we compare the results of the laboratory and numerical experiments in § 10.

2. Governing equations

In deriving our continuum model of the mushy layer, we will be assuming that each infinitesimal volume contains solid and pore fluid (except in the melt region where there is only pore fluid) and that the solid and liquid phases are in thermodynamic equilibrium. The non-dimensional equations describing enthalpy and solute conservation in a reactive porous medium are (Worster 1992, 2000)

$$\overline{\rho c_p}\frac{\partial \theta}{\partial t} + \boldsymbol{u}\cdot\nabla\theta = \frac{1}{Ra}\nabla\cdot[\bar{k}\nabla\theta] + S\frac{\partial \phi}{\partial t} \tag{2.1}$$

and

$$(1-\phi)\frac{\partial C}{\partial t} + \boldsymbol{u}\cdot\nabla C = \frac{\epsilon}{Ra}\nabla\cdot[(1-\phi)\nabla C] + \rho_s(C-\mathscr{C})\frac{\partial \phi}{\partial t}. \tag{2.2}$$

Here, $\boldsymbol{u}$, θ, C and ϕ are all non-dimensional variables and represent, respectively, the Darcy (or transport) velocity of the fluid, which we will assume to be two-dimensional;

the temperature of the fluid and matrix; the concentration of solute in the fluid; and the volume fraction that is occupied by solid (hereinafter called the solid fraction). The relationships between the non-dimensional and dimensional temperature and concentration are given by $\theta = (T - T_0)/\Delta T$ and $C = (C_d - C_0)/\Delta C$, where T and C_d are the dimensional temperature and concentration with $\Delta T = T_w - T_0$ and $\Delta C = C_w - C_0$. The height of the tank, H, and $H^2/(\kappa_l Ra)$ are used as the length and time scales, where κ_l is the thermal diffusivity of the liquid (assumed to be independent of temperature and concentration) and $Ra = [\rho_{ld} g \Pi_0 H \beta (C_w - C_0)]/(\kappa_l \mu_l)$ is a compositional, porous-medium Rayleigh number. The variables ρ_{ld}, g, Π_0 and μ_l represent the dimensional density of the liquid, the acceleration due to gravity, the dimensional permeability of the porous medium when $\phi = 0$, and the dynamic viscosity of the liquid, respectively. The variable $\beta = \rho_{ld}^{-1}(\partial \rho_{ld}/\partial C)$ is the equivalent of the thermal expansion coefficient, α, for composition. We scale time with the diffusion time divided by the Rayleigh number because the dynamics of the system are controlled mostly by convection, and consequently the diffusion time is a unit of time that is significantly too long for most cases. The dimensionless heat capacity and thermal conductivity for a small volume containing solid matrix and liquid are defined by the appropriate averages, $\overline{\rho c_p} = \rho_s c_{ps} \phi + (1 - \phi)$ and $\overline{k} = \phi k_s + (1 - \phi)$ where ρ_s, c_{ps} and k_s are the density, heat capacity and thermal conductivity of the solid expressed in units of the liquid values for these same quantities. The diffusivity ratio, also called the Lewis number or inverse Schmidt number, is defined as $\epsilon = D/\kappa_l$, where D is the diffusion coefficient of the solute and κ_l is the thermal diffusivity of the liquid. The dimensionless parameters $\mathscr{C} = (C_s - C_0)/\Delta C$ and $S = \rho_s L/(c_{pld} \Delta T)$ are the concentration ratio and Stefan number where L and c_{pld} are the dimensional latent heat of freezing and the heat capacity of the liquid. The parameter $\mathscr{C}$ describes the amount by which the liquid solute concentration changes owing to a given degree of melting or solidification while S describes the strength of latent heating. From left to right, the terms in equation (2.1) represent: the change in internal energy per unit volume in both the liquid and the solid; the heat energy transported by liquid advection; the heat transported by conduction through both the liquid and the solid; and the latent heating due to melting or freezing. Similarly, terms in equation (2.2) represent: the change in the concentration of solute in the liquid; the advection of the solute by motion of the liquid; the transport of solute by diffusion through the liquid; and the change in the concentration of solute in the liquid owing to melting and freezing.

In the mushy region, we assume that the liquid and solid are in thermodynamic equilibrium and hence the fluid has the liquidus concentration which we approximate by a linear relationship. This condition becomes

$$\theta = C \tag{2.3}$$

when we scale temperature and concentration as described above. In the melt region, no such relation between temperature and concentration exists and they evolve separately.

The ratio of the terms that multiply the time derivatives of the solid fraction in equations (2.1) and (2.2) is an important parameter in determining the evolution of the system. If $S/[\rho_s(C - \mathscr{C})] \ll 1$ then the solute concentration will change much more rapidly with a given change in the solid fraction than will the temperature. In this limit, the melting or solidification that is necessary to maintain the liquidus condition will result in a significant change in the solute concentration with only a small change in the temperature. In a system of this type, throughout most of the mushy region,

the transport of the solute and heat will be mostly governed by equation (2.1). In the opposite limit, the melting or solidification will result in a large change in the temperature with a small change in the solute concentration and the transport of solute and heat will mostly be governed by (2.2).

Darcy's law,

$$\boldsymbol{u} = -\Pi[\nabla p + \rho_l k]/(\beta \Delta C), \tag{2.4}$$

is used to describe the force balance for flow in the reactive porous medium, where p is the pressure and k is an upward pointing unit vector. In the calculation to be presented, the non-dimensional permeability Π is assumed to be isotropic and to vary with solid fraction according to

$$\Pi = (1-\phi)^3. \tag{2.5}$$

Power-law relationships between permeability and solid fraction are commonly used in modelling work (Worster 1992) and give a strong nonlinear relationship between solid fraction and permeability. They are also a slightly simplified versions of the Kozeny–Carmen relationship (Carmen 1939). In real systems, the permeability may also be a function of the area of pore spaces per unit volume and of the connectivity of the porous network. Analysis characterizing the importance of these effects is ongoing (e.g. Martys, Torquato & Bentz 1994; Saar & Manga 2002).

The variation of the non-dimensional liquid density with temperature and concentration is expressed as

$$\rho_l = (1 - \alpha \Delta T \theta + \beta \Delta C\ C). \tag{2.6}$$

We assume that variations in the liquid density owing to composition and temperature are significant only in the buoyancy term of Darcy's law and hence make the Boussinesq approximation.

Mass conservation is expressed as

$$\frac{\partial \bar{\rho}}{\partial t} + \nabla \cdot (\rho_l \boldsymbol{u}) = 0, \tag{2.7}$$

where $\bar{\rho} = \rho_s \phi + (1-\phi)$. In what follows, we will assume that the solid fraction melts sufficiently slowly compared with the fluid velocity that this equation can be adequately approximated by the incompressibility condition $\nabla \cdot \boldsymbol{u} = 0$. This allows us to introduce a streamfunction such that $\boldsymbol{u} = (\partial_z \psi, -\partial_x \psi)$. Taking the curl of the Darcy equation (2.4) and using (2.6), we obtain the following Poisson equation for the streamfunction

$$\frac{\partial^2 \psi}{\partial x^2} + \frac{\partial^2 \psi}{\partial z^2} = -\frac{3}{1-\phi}\left(\frac{\partial \phi}{\partial z}\frac{\partial \psi}{\partial z} + \frac{\partial \phi}{\partial x}\frac{\partial \psi}{\partial x}\right) - (1-\phi)^3\left(-\frac{\partial C}{\partial x} + \frac{\alpha \Delta T}{\beta \Delta C}\frac{\partial \theta}{\partial x}\right). \tag{2.8}$$

The density of the fluid generally depends much more strongly on concentration than on temperature and we have assumed a value of $(\alpha \Delta T)/(\beta \Delta C)$ of 0.1. We have placed the terms due to the solid fraction dependence of the permeability on the right-hand side of the equation. This will facilitate the numerical solution of the equation because the coefficients on the left-hand side of the Poisson equation will have to be initialized only once at the beginning of the simulation. We are forced to iterate the solution to convergence, however.

Equations (2.1), (2.2), (2.8) and (2.3) form a closed set for θ, C, ϕ and ψ within the mushy region. In the melt region, $\phi = 0$ and somewhat simplified forms of (2.1) (2.2) and (2.8) apply. Because the interface between these regions evolves with time, this

Symbol	Name	Definition	Estimate for experimemt	Used
Ra	Rayleigh number	$(\rho_{ld} g \beta \Delta C \Pi_o H)/(\kappa_l \mu_l)$	15 000	100–2500
S	Stefan number	$(\rho_{sd} L)/(\rho_{ld} c_{pld} \Delta T)$	5.9	5.9
ϵ	Diffusivity ratio	D/κ_l	< 0.01	0.1
$\mathscr{C}$	Concentration Ratio	$(C_s - C_0)/\Delta C$	3.45	3.45
ρ_s	Density ratio	ρ_{sd}/ρ_{ld}	2.109	2.109
c_{ps}	Heat capacity ratio	c_{psd}/c_{pl}	0.22	0.22
k_s	Conductivity ratio	k_{sd}/k_l	?	1
ϕ_0	Initial solid fraction		0.44	0.44

TABLE 1. Summary of non-dimensional parameters. All quantities in the definition of the non-dimensional parameters are dimensional. A subscript d is used to distinguish dimensional parameters from similar non-dimensional ones.

problem represents a moving-boundary problem (Crank 1984; Shyy *et al.* 1995). There are essentially two approaches to solving such problems numerically. One involves solving the system separately in each region and then matching the solutions and possibly their derivatives at the interface as boundary conditions. The position of the interface must then be calculated and, as it undulates, coordinate transformations must be applied to both solution regions. The second approach, which is the one we follow here, involves defining a set of equations that are valid in both regions and solving all equations on a single fixed grid. The position of the interface can be determined after the calculation as the boundary of the region in which $\phi = 0$. We will outline the algorithm for the solution of this problem in § 4.

3. The simulation

All of the calculations were initiated with a uniform solid fraction, $\phi_0 = 0.44$, as in the experiments of Hallworth *et al.* (2004), except for two with $\phi_0 = 0.1$ and 0.6 that were performed to investigate the effects of varying this parameter. The non-dimensional temperature and concentration were set to 0 throughout the solution region. The outer boundary conditions consisted of a condition of no mass flux ($\psi = 0$) and no flux of solute on all boundaries as well as a condition of no heat flux through the lower and side boundaries. The top boundary temperature was fixed at 1 at the beginning of the simulation to initiate melting and thereafter maintained at that value.

The dimensions of the solution medium were scaled to be 30 cm × 39 cm horizontally and vertically. The values of the non-dimensional parameters used are shown in table 1. Note that, for numerical reasons, the value of ϵ used in the convection experiments was 0.1 while the real value is about ten times smaller. We also use $k_s = 1$ for the sake of simplicity. Model runs were performed with Rayleigh numbers of 100, 250, 500, 1000 and 2500, with 2500 being the largest value that we could integrate in a practical way at this time. A further set of simulations was performed using $Ra = 1000$ and various values of $\mathscr{C}$.

Given the parameters in table 1, the ratio $S/[\rho_s(C - \mathscr{C})]$ varies from 0.81 to 1.08 during the course of a simulation since C varies from 0 to 1. As a result, melting and solidification result in changes in solute concentration and temperature that are of similar magnitude.

4. Numerical method

The equations are solved in a two-dimensional Cartesian domain. The resolutions used were 145×145 for the conduction simulations and for the convection simulations with Rayleigh numbers of 100, 175, 250 and 500. The simulation with $Ra = 1000$ employed a resolution of 289×289, while the simulation with $Ra = 2500$ was integrated with a 577×577 grid for the first half of the simulation, which was then interpolated onto a 145×145 grid for the second half. The simulation with $Ra = 2500$ took more than a month of computing time. High resolution was required because of the rapid variation in the solute concentration field in the vicinity of the mush–liquid interface. Some trial and error was necessary in order to determine adequate resolution. The streamfunction was calculated using a second-order accurate multi-grid solver (Adams 1991).

Equations (2.1), (2.2) and (2.8) all reduce to equations valid in a passive porous medium when $\phi = 0$ and as such are applicable in the entire domain. The significant challenge involves updating the solid fraction field as the evolution of this quantity is implicitly defined by (2.1), (2.2) and (2.3). In physical terms, the melting of the solid fraction in a small volume of the solution domain can be thought of in the following way. If the frozen solute becomes immersed in fluid whose temperature is greater than the liquidus temperature for its concentration, then some quantity of the frozen solute will melt. In melting, the concentration of solute in the fluid increases and the temperature of the fluid decreases owing to the effects of latent heat. The magnitude of the change in solute concentration owing to a given degree of melting is parameterized through $\mathscr{C}$ while the strength of the latent heating effect is described by S. If there is sufficient solid within the volume that the concentration and temperature can be brought to the liquidus by melting, then the solid fraction will decrease with some solid fraction remaining. If there is insufficient solid fraction, then the solid will melt completely and the temperature and the concentration will evolve separately.

Numerically, we discretize (2.1) and (2.2) using centred finite differences. The advection terms are calculated using the Arakawa Jacobean (Arakawa 1966). The second derivatives in the diffusion terms, such as $\partial^2\theta/\partial x^2$, are approximated by expressions of the form $(\theta^n_{i+1,j} - \theta^{n+1/2}_{i,j} - \theta^{n-1/2}_{i,j} + \theta^n_{i-1,j})/\Delta x^2$. Here i and j are indices referring to the x and z position in the grid, n is an index over time steps and Δx is the (uniform) grid spacing in the x-direction. The discretized forms of (2.1) and (2.2) can then be written as

$$\theta^{n+1/2}_{i,j} = \Theta_1 + \Theta_2\left(\phi^{n+1/2}_{i,j} - \phi^n_{i,j}\right) \tag{4.1}$$

and

$$C^{n+1/2}_{i,j} = CON_1 + CON_2\left(\phi^{n+1/2}_{i,j} - \phi^n_{i,j}\right). \tag{4.2}$$

Here, Θ_1, Θ_2, CON_1 and CON_2 are all quantities that can be calculated from finite differences of fields known at the nth time step (the full forms of these quantities are given in the Appendix). We can then solve for the solid fraction required in time step $n + 1/2$ in order for the liquidus condition to be achieved,

$$\phi_{req} = \phi^n_{i,j} + \frac{CON_1 - \Theta_1}{\Theta_2 - CON_2}. \tag{4.3}$$

If $0 < \phi_{req} < 1$ based on this calculation, then we set $\phi^{n+1/2}_{i,j} = \phi_{req}$. If $\phi_{req} \leqslant 0$, then $\phi^{n+1/2}_{i,j}$ is set to 0. In either case, the new $\phi^{n+1/2}_{i,j}$ is used in (4.1) and (4.2) to calculate the new temperature and concentration fields. Note that if $0 < \phi^{n+1/2}_{i,j} < 1$, then $\theta = C$ and

the liquidus condition will be satisfied, whereas if $\phi_{i,j}^{n+1/2} = 0$, then the concentration and temperature fields evolve independently.

The numerical code was tested by comparing its predictions for the critical Rayleigh number for the onset of convection with the linear theory presented in Worster (2000). For the sake of these tests, the aspect ratio of the box was set to 1, the lower and upper boundaries were made to have constant temperatures of 0 and 1, respectively, and the initial conditions were taken to be those of constant solid fraction, a conduction profile in the temperature and with liquidus solute concentration. An initial perturbation of the form $2\gamma\pi\cos(\pi x)\sin(\pi z)$ was introduced for the temperature and solute concentration fields and $\gamma\sin(\pi x)\cos(\pi z)$ for the streamfunction where γ was an arbitrary small parameter. It was then observed whether this perturbation grew or decayed. The linear theory is greatly simplified if we assume that $\mathscr{C} \gg 1$ and that $k_s = 1$ and either $\phi_0 \ll 1$ or $\epsilon = 0$. In these cases, equations (2.1) and (2.2) can be combined to eliminate the terms in $\partial\phi/\partial t$ and the resulting equations have the same form as those for a homogeneous non-reactive porous medium. Under these assumptions, the critical Rayleigh number becomes

$$Ra_c = 4\pi^2 \frac{\left(1 + \dfrac{S\epsilon}{\rho_s \mathscr{C}}\right)}{\left(1 + \dfrac{S}{\rho_s \mathscr{C}}\right)(1-\phi_0)^3 \left(1 - \dfrac{\alpha \Delta T}{\beta \Delta C}\right)}. \tag{4.4}$$

All of the parameters in (4.4) were varied and as long as the assumptions described above were valid, the agreement between the predictions and the numerical model were good to better than 0.5 %. The critical Rayleigh number for these boundary and initial conditions was also found for the values of the parameters given in table 1 (note that in this case $\mathscr{C}$ is of order 1 so (4.4) is not valid) and was found to be 134. The boundary and initial conditions used in the simulations, which are described in § 3, are different and the convection is transient so the Rayleigh number for the onset of convection will be somewhat different, but this value gives us an estimate of the magnitude of this parameter. Note also that this critical Rayleigh number is much greater than $4\pi^2$ largely because Ra is defined in terms of the permeability when $\phi = 0$.

Solute and energy balances for the entire domain were also monitored and found to be satisfied to within a few per cent, even for long integrations. Also, simulations with Rayleigh number 500 were repeated with resolutions of 145×145, 289×289 and 577×577. The agreement in all quantities after a long integration was better than 1 %. The only small qualitative difference in the simulations was that the interface began to descend earlier in higher-resolution simulations since the solid fraction field was divided into thinner layers.

5. Simple model

In this section, we will examine relationships between various volume-averaged quantities and use these to develop a simple model that can be used to predict the final solid fraction, ϕ_f, the final solute concentration, C_f, and the average height of the mush–liquid interface as a function of time, $h(t)$. We develop this simple model in terms of the non-dimensional parameters, ϕ_0, S, $\mathscr{C}$, ρ_s, c_{ps} and Ra that characterize the numerical model. The simple model is valid when solute is mixed rapidly throughout the entire system and its results are useful in aiding our understanding of the more detailed numerical model.

Owing to the boundary condition of no flux of solute through the outer boundaries, the total amount of solute in the domain is fixed and can only be transferred between solid and liquid forms. If we integrate (2.2) over the entire domain and further assume that owing to rapid mixing throughout the system, the spatial correlation of ϕ and C is negligible, we derive the equation relating the volume-averaged solid fraction, $\langle\phi\rangle$, and the volume-averaged liquid solute concentration, $\langle C\rangle$ (where $\langle\ \rangle$ indicates a volume average over the domain)

$$\frac{1}{\mathscr{C}-\langle C\rangle}\frac{\partial\langle C\rangle}{\partial t}=\frac{-\rho_s}{(1-\langle\phi\rangle)}\frac{\partial\langle\phi\rangle}{\partial t}. \tag{5.1}$$

We write the solution to (5.1) with the initial condition $\langle\phi\rangle=\phi_0$ when $\langle C\rangle=0$ as

$$\langle\phi\rangle=\phi_0+(1-\phi_0)\left[1-\left(\frac{\mathscr{C}}{\mathscr{C}-\langle C\rangle}\right)^{1/\rho_s}\right]. \tag{5.2}$$

Our numerical method does not allow for a change in volume of the domain when the material changes phase, which will happen in the real system if $\rho_s\neq 1$ (Chiareli, Huppert & Worster 1994). If this volume-changing effect were taken into account, then the final average solid fraction could be calculated by equating the final and initial bulk concentrations. The final volume-averaged solid fraction predicted by this procedure is

$$\phi_f=\frac{\bar{C}_0-1}{\rho_s(\mathscr{C}-\bar{C}_0)+(\bar{C}_0-1)}, \tag{5.3}$$

where $\bar{C}_0$ is the non-dimensional initial bulk concentration. Equations (5.2) (with $\langle C\rangle=1$) and (5.3) predict final average solid fractions of 0.34 and 0.30, respectively, for the parameters used here. While this difference is not entirely insignificant, the qualitative description of the behaviour of the system described here will not be significantly affected. The condition for there to be solid remaining at the end of the simulation is that $\langle\phi\rangle>0$ when $\langle C\rangle=1$. If (5.2) returns a value for $\langle\phi\rangle$ that is less than 0 when $\langle C\rangle=1$, then we know that the final state will be one of complete melt and we can predict the final value of the liquid concentration by setting $\langle\phi\rangle=0$ and solving (5.2) for $\langle C\rangle$ to obtain

$$\langle C_f\rangle=\mathscr{C}[1-(1-\phi_0)^{\rho_s}]. \tag{5.4}$$

Given the rest of the parameters in table 1, the initial solid fraction that is necessary for there to be solid remaining at the end of the simulation is 0.15.

Integrating the enthalpy equation over the volume of the domain and time, using the boundary conditions that there be no heat flux through the side or bottom boundaries and assuming that the variation in $\overline{\rho c_p}$ is small, we arrive at

$$\langle\phi\rangle=\phi_0+\langle\theta\rangle\frac{\overline{\rho c_p}}{S}-\frac{1}{RaV}\int_0^t Q_s(t')\ \mathrm{d}t', \tag{5.5}$$

where $Q_s(t)$ is the unknown conductive heat flow from the surface boundary and V is the volume of the domain. These forms for $\langle\phi\rangle$ were compared with the results of the numerical calculations (not shown) and were found to be in good agreement, providing useful tests of the numerical code. Note that since we can calculate $\langle\phi\rangle$ from (5.2), we can calculate the integrated surface heat flow. For the time to equilibration, the total energy that goes into increasing the temperature of the system is approximately

$\overline{\rho c_p}$ while the energy used to overcome the latent heat of melting is $S(\phi_0 - \phi_f)$. The ratio of these quantities is 1.3 for this system.

It is worth noting that the final amount of solid remaining depends only on parameters in the solute conservation equation whereas the parameters that appear in the enthalpy conservation equation affect only the time-scale to equilibration. If the boundary conditions were changed such that the surface was insulating, but solute could diffuse into the domain, then enthalpy rather than mass of solute would be conserved in the system and ϕ_f would depend on S and $\overline{\rho c_p}$ while $\mathscr{C}$, ρ_s and ϵ would affect only the time scale to equilibration.

Although we can predict the total amount of solid that will remain in the final state, as well as the final concentration and temperature, from considerations of solute and energy conservation alone, we must understand the transport properties of the system in order to predict the final position of the interface. There are two extreme modes of melting that can take place as the system equilibrates. One is complete melting of the solid at the interface, which results in the interface descending, while the other involves melting in the bulk of the solid, with no motion of the interface. As heat diffuses into the system from the surface, melting occurs at the interface resulting in an increase in the liquid solute concentration. If this solute is not transported away, then gradual melting will take place as the temperature increases and the surface thermal boundary layer will penetrate into the bulk of the material. In this case, if there is any solid left at the end of the simulation (determined by whether the temperature at the upper surface is above or below the liquidus temperature for the bulk concentration), then the final state will be one with not only constant temperature and solute concentration, but uniform solid fraction as well. This is the case when there is no convection and the solute diffusivity ϵ is set to 0. If the surface temperature is above the liquidus temperature for the bulk concentration then a region of complete melt will form and a melt front will advance through the domain until the domain is completely molten. Similarity solutions for melting in a mushy layer in the absence of solute transport for a semi-infinite layer were presented by Feltham & Worster (2000).

Alternatively, if solute can be transported into the bulk and away from the interface, then the interface region will require further melting in order to increase the solute concentration and remain in equilibrium. This runaway melting results in the formation of an interface when a layer has been completely melted. The liquid that is transported into the bulk of the material will be relatively solute rich and, as it cools, it will have to freeze onto the matrix, increasing the solid fraction in the bulk and increasing the temperature. Note that with rapid mixing of solute throughout the mush, its temperature will be essentially uniform and hence the thermal boundary layer from the surface will be confined to the melt region, resulting in all of the energy from the surface heat flow being used to melt the interface region. The amount that the interface descends increases as the efficiency with which solute can be transported away from the interface region increases. There is a limit on the displacement of the interface, however, which is due to the limiting rate at which heat can be transported by conduction across the upper melt region. Kerr (1994*a*, *b*) published simple scaling expressions for melting driven by compositional convection where melting and dissolution were limited only by the rate at which convection could remove solute and supply heat to a solid block. In our case, in the limit that solute is transported away from the interface much faster than heat can diffuse down across the upper melt region, all of the energy from the surface heat flow will be used to cause melting at the interface. In this limit, the energy balance of the system can

be split into two equations. The surface heat flow is balanced by the melting at the interface, which for the case of a sharp interface can be written

$$Q_s = S\phi_m \frac{\partial h}{\partial t}, \tag{5.6}$$

where ϕ_m is the solid fraction in the mushy layer. Also, the change in temperature in the lower layer is balanced by the latent heat released by the freezing of solute onto the matrix,

$$\overline{\rho c_p}\frac{\partial \theta_m}{\partial t} = S\frac{\partial \phi_m}{\partial t}, \tag{5.7}$$

where θ_m is the temperature in the mush. Integrating this second equation and assuming no variation in $\overline{\rho c_p}$, we obtain

$$\phi_m = \phi_0 + \frac{\overline{\rho c_p}}{S}\theta_m. \tag{5.8}$$

If the interface is sharply defined, we can also write

$$\phi_m h = \langle \phi \rangle, \tag{5.9}$$

which allows us to predict the final average interface height. For the parameters used in our simulation, we obtain a value of $h_f = 0.60$.

In order to build a simple model of the time variation of the position of the interface, we approximate $Q_s(t)$ in (5.6) as the heat flow due to a linear conduction profile in the melt region where we assume that there is negligible motion owing to the stable density stratification in this region and we obtain the following non-dimensional equation

$$\frac{1}{Ra}\frac{1-\theta_m}{1-h} = S\phi_m \frac{\partial h}{\partial t}. \tag{5.10}$$

Combining (5.2), (5.8) and (5.9), we obtain

$$h\left(\phi_0 + \frac{\overline{\rho c_p}}{S}\theta_m\right) = \phi_0 + (1-\phi_0)\left[1 - \left(\frac{\mathscr{C}}{\mathscr{C}-\theta_m}\right)^{1/\rho_s}\right]. \tag{5.11}$$

The assumption that the evolving temperature profile can be approximated as a straight line requires that $\partial h/\partial t \ll \kappa_l/(1-h)$ which will be the case when either ϕ_0 or S is large, as we will demonstrate below. Here, we have assumed that $\langle C \rangle$ can be approximated as θ_m in (5.2). This assumption is valid when either the interface does not descend very much or the solute is uniformly distributed throughout the entire domain.

Figure 3(a) presents the numerical integration of (5.10) with a numerical solution for θ_m from (5.11) at each time step (solid lines). The values of the non-dimensional parameters are those presented in table 1. We also show a solution from the numerical model in which the effects of convection have been mimicked by setting the solute diffusivity, ϵ, to the very high value of 100 (dashed line). Although $\epsilon \ll 1$ for all real physical systems, this device allows us to investigate a model in which solute can be rapidly removed from the region of the interface in a computationally efficient manner. A value of $\epsilon = 100$ is sufficiently large that increasing this value will not result in any further change in the behaviour of the system, as we will demonstrate later in the discussion of figure 4. It can be seen that the agreement between the two models is very good, with the simple model overestimating the change in the interface height only slightly. The good agreement between the results of the two models indicates that, for such a large value of solute diffusivity, all of the heat

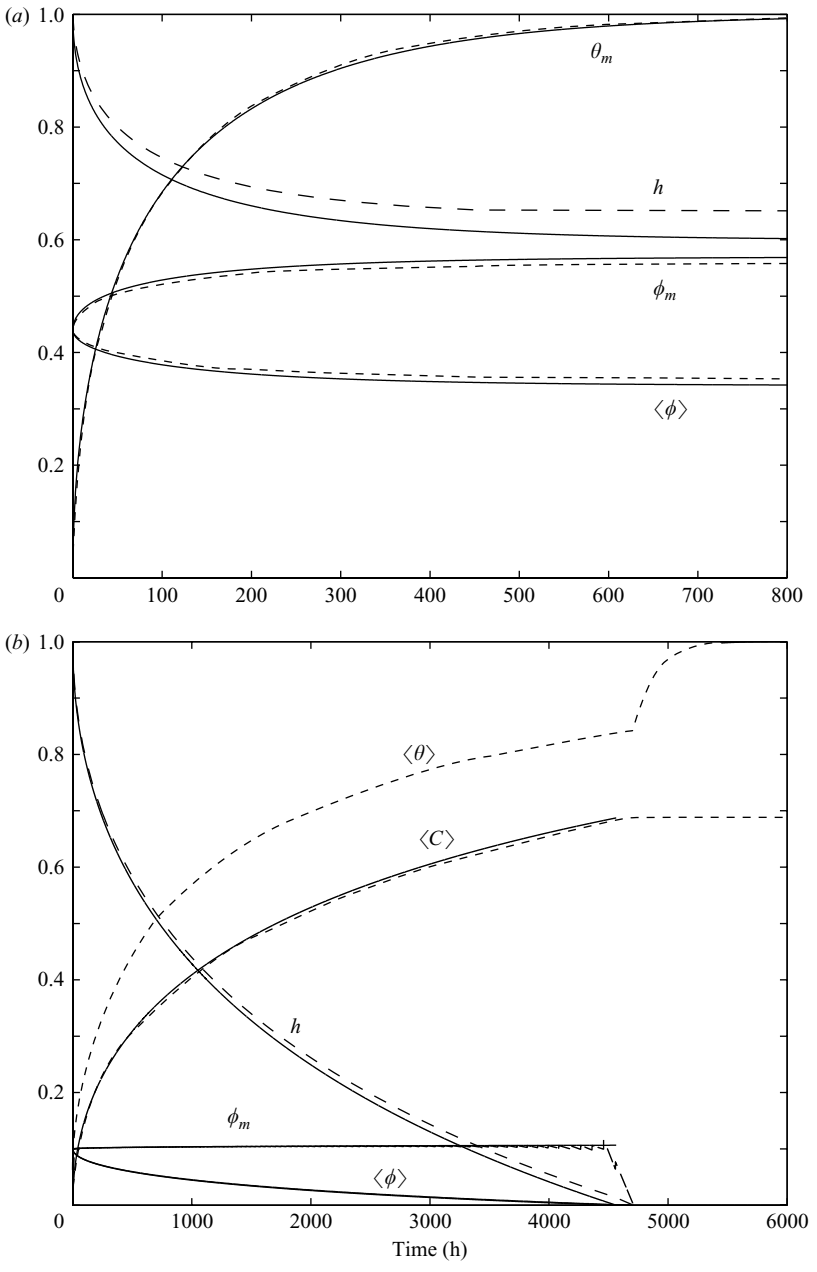

FIGURE 3. Curves of comparison between the results of the numerical model with the effects of convection mimicked by using a large solute diffusivity (dashed) with the predictions of the simple analytical model (solid curves) for the interface height h, the average temperature in the mushy region θ_m, the average solid fraction in the mushy region ϕ_m, and the average solid fraction in the entire domain $\langle\phi\rangle$. (*a*) $\epsilon = 100$. Other parameters as in table 1. (*b*) $\phi_0 = 0.1$, $S = 100$ and $\epsilon = 100$. Other parameters as in table 1.

conducted from the surface goes towards melting at the interface, while the energy balance in the interior of the mush is between latent heat due to solidification and the increase in temperature of the material. In this case $\phi_m > \phi_0$, indicating that the solid fraction in the mush region has increased over its initial value.

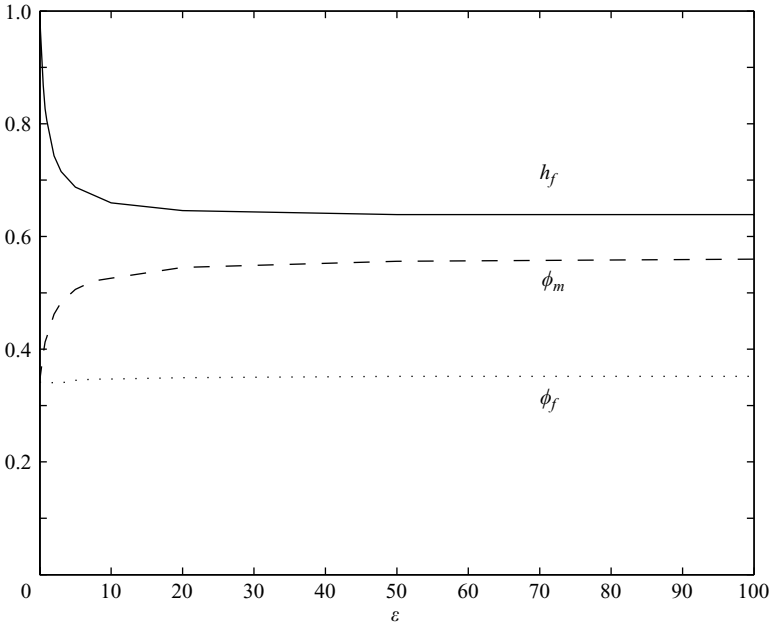

FIGURE 4. The final interface height h_f, average solid fraction ϕ_f, and average solid fraction in the mush ϕ_m, in integrations suppressing convection as a function of the non-dimensional solute diffusivity ϵ.

We present in figure 3(b) a similar comparison of the two models with the initial solid fraction, ϕ_0, set to a small value of 0.1 which is less than the minimum value of 0.15 required for there to be a solid fraction remaining at the end of the simulations for the values of ρ_s and $\mathscr{C}$ used. We have also increased the value of S substantially to 100 in order to decrease the rate of motion of the interface to the point that the heat flow can be approximated adequately by that of a linear conduction profile in the melt region. This accounts for the greatly expanded time scale and for the small variation in the average solid fraction in the mushy region. The agreement between the results of the two models is again very good. In this case, the average solid fraction and the interface height decrease to 0 at a time of roughly 4700 h. The average solid fraction in the mushy region goes precipitously to 0 at this time in the numerical conduction calculation. We display the volume-averaged concentration $\langle C \rangle$ rather than the average temperature in the mushy layer θ_m, although these quantities are essentially identical until the time that the solid has completely melted. We also display the volume-averaged temperature for this calculation. It can be seen that the average concentration is constant and less than 1 after complete melting has occurred. Equation (5.4) predicts a value of 0.684 while the final concentration in the numerical calculation is 0.688. The volume-averaged temperature, $\langle \theta \rangle$, rises rapidly to 1 after the system has completely melted since no further heat energy is required to overcome the latent heat of melting which is very large when a large value of S is used.

In figure 4, we present the variation of the final equilibrated values of h, ϕ_m and ϕ_f as a function of ϵ for numerical simulations without the effects of convection with an initial value of $\phi_0 = 0.44$ and $S = 5.9$. It can be seen that rapid removal of solute from the interface region is obtained for a value of ϵ roughly in excess of 15. For values less than this, the interface does not descend as far during the simulation and

the solid fraction in the mushy layer does not increase as much, whereas for values of $\epsilon < 1.5$, the final value of $\phi_m < \phi_0$. This indicates that there is appreciable melting in the interior of the mush owing to the heat diffusing from the surface boundary. The volume-averaged final solid fraction, ϕ_f, does not depend on the transport properties of the system (only the final distribution of ϕ and hence h and ϕ_m does) and as expected, ϕ_f is essentially unchanged as a function of ϵ. The small variation in ϕ_f is due to a small degree of numerical error. For simulations in which convection is taking place, it is expected that even with a small value of ϵ, the interface should descend appreciably owing to the transport of solute by convection. Although we will show this to be the case in the next section, even the highest Rayleigh-number simulation that we undertook was not in the limit where all of the melting was at the surface, as is the case when $\epsilon > 15$.

It should be mentioned that the assumptions that ϕ and C are not spatially correlated and that $\langle C \rangle = \theta_m$, which are incorporated into the derivation of the simple model presented here, are particularly well satisfied when ϵ is large. High solute diffusivity will result in a solute concentration that does not vary spatially and so will be uncorrelated with the solid fraction field. Similarly, $C = \theta_m$ in the mushy region owing to the liquidus constraint, and in the melt region as well if the diffusion of solute is very large. Hallworth *et al.* (2004) presented a similar simple theory to explain the motion of the interface in their experiments that is valid in the limit that $\epsilon = 0$ and that convective transport of solute is sufficiently rapid that all of the heat entering the system at the top causes melting at the interface. Owing to the lack of solute diffusivity and the stable stratification and hence lack of convective transport in the melt region, the solute concentration in the melt region of their model decreases monotonically from the melt–mush interface where its value is θ_m to 0 at the top. The concentration at a given height is the liquidus concentration appropriate to the temperature that obtained when the interface was at that height. Consequently, their model has significantly less solute in the melt region and more in the mush region than the simple model presented here. Owing to the effects of thermal diffusion, the predicted final temperature in their model was also uniform and equal to 1 and hence the predicted final solid fraction in the mush, ϕ_m, is the same as in the simple model here. As a result, the predicted final interface height in their model for the non-dimensional parameters presented here is 0.67, a value somewhat larger than the result of 0.6 for the simple model of this section. The experiments cannot be run long enough to confirm the former value.

In the results of the numerical model with the effects of convection included that we will present in the following section, there is also a significant degree of compositional stratification in the melt region, as we will demonstrate in § 9. However, owing to the non-zero solutal diffusivity that is used in these calculations ($\epsilon = 0.1$), the final state is still one of constant solutal concentration. As a result, C is only constant throughout the domain at the very beginning and end of the simulation, and the assumptions that go into the derivation of the simple model are only valid at those times. Similarly, the assumption of rapid mixing of solute from the interface into the mush which will result in all of the heat from the surface being used to cause melting at the interface is only valid during the early, vigorous convective phase of the simulation.

6. Results 1. Comparison of different Rayleigh number simulations

In figure 5, we present the volume-averaged kinetic energy for convection calculations with Rayleigh numbers 250, 500, 1000, and 2500 and all other parameters

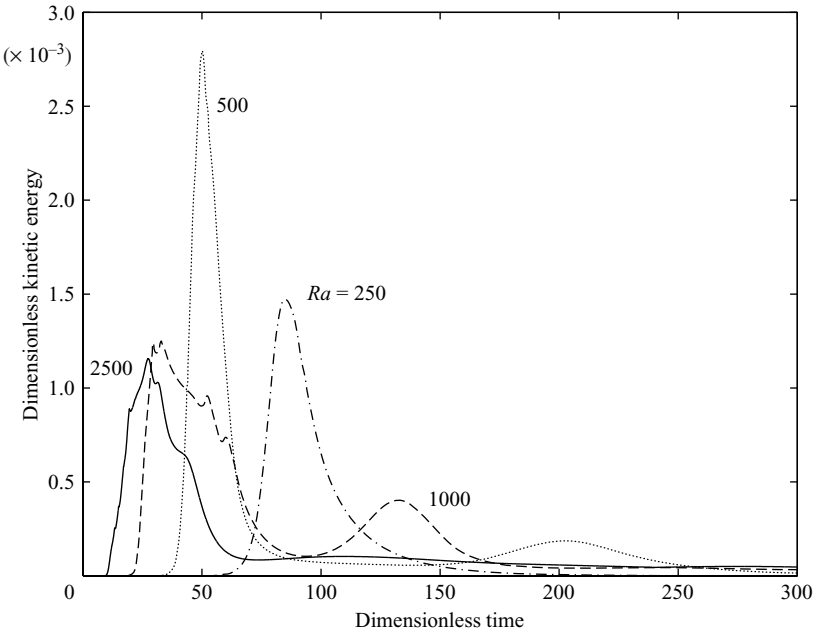

FIGURE 5. Volume-averaged kinetic energy as a function of time for four simulations with different Rayleigh numbers. Kinetic energy and time are both non-dimensional as described in the text.

are as given in table 1. The time is non-dimensional in order to be able to compare all of the simulations on the same figure. Time is scaled inversely with the Rayleigh number and as a result, processes take place faster for higher Rayleigh numbers. Similarly, the amplitude is non-dimensional and should be scaled by Ra^2 to obtain the dimensional amplitudes; it is for this reason that the simulation with $Ra = 500$ appears to have the largest amplitude, whereas if the kinetic energies were scaled, the peak kinetic energy with $Ra = 2500$ would be roughly 8 times greater than the peak kinetic energy for the simulation with $Ra = 500$. In the early stages of the simulation; (less than 2 h of simulated time for the case of $Ra = 2500$), there is no motion. During this time, heat is diffusing into the top of the system. An instability sets in once the thermal boundary layer at the surface reaches a critical depth, dependent on the Rayleigh number. The initial instability is confined to the region of the thermal boundary layer and consists of rolls of roughly unit aspect ratio. However, the instability quickly rearranges itself to fill the entire volume. The early instability is extremely intense owing to the large buoyancy contrast between the heavy solute-rich material at the interface and the material in the interior. The material in the interior is quickly brought to the higher temperature and concentration of the surface by convective mixing and the kinetic energy decreases substantially. For the case of $Ra = 250$, the critical thermal boundary-layer thickness amounts to almost the entire depth of the porous medium and the initial instability consists of only a single roll. Once mixing has reduced the buoyancy contrast between the liquid at the interface and in the mush for $Ra = 250$, the system is no longer convectively unstable and the kinetic energy decreases to 0. For the case of $Ra = 500$, the intense early spike in kinetic energy corresponds to a mode with two rolls. The secondary bump that

occurs at time 200 corresponds to a time when the convection has switched from two rolls to a single roll. After this instability, the kinetic energy gradually decays to 0 as the system equilibrates to a uniform temperature and concentration. For the cases with $Ra = 1000$ and $Ra = 2500$, the first instability corresponds to many rolls as the critical boundary-layer thickness is achieved while the surface thermal boundary layer is still quite thin. A series of transitions then take place in which the number of rolls decreases. These events correspond to the various bumps that can be seen on the kinetic energy curves. The results of the analogue experiments also indicate a series of rearrangements of the flow pattern as the dissolution progressed. Simulations were also undertaken with Rayleigh numbers of 100 and 175. The kinetic energy for the $Ra = 100$ case never increased appreciably from 0 whereas there was a short period of very weak convection for the $Ra = 175$ case, indicating that the critical Rayleigh number for this system is between 100 and 175 which is similar to the critical Rayleigh number of 134 listed in § 4 for convection with isothermal top and bottom boundaries and an initial thermal conduction profile. In what follows, we will use 125 as an estimate of the critical Rayleigh number, Ra_c, for this system and list the ratio of Ra/Ra_c in order to indicate more explicitly the degree of convective forcing.

In figure 6(a) we present the non-dimensional volume-averaged temperature as a function of dimensional time for simulations with different values of the Rayleigh number and for a purely conductive simulation. A value of $\kappa_l = 10^{-3}\,\mathrm{cm}^2\,\mathrm{s}^1$ which is approximately the thermal diffusivity of aqueous potassium nitrate for the concentrations considered in Hallworth *et al.* (2004) is used in order to calculate the time scale. During the early stages, before the onset of a convective instability, all of the simulations evolve in the same manner as the purely conductive simulation. Once convection begins, there is a very rapid rise in the average temperature as hot dense material from the descending interface flushes through the bulk of the system and cold material from near the base is brought up in contact with the hot upper surface. After the period of intense mixing, the system settles to a gradual approach to equilibrium with the upper surface. For the case of $Ra = 250$ or $Ra/Ra_c = 2$, this approach phase is entirely conductive.

The volume-averaged solid fraction for the same simulations is shown in figure 6(b). We also plot the final solid fraction ϕ_f as predicted by (5.2), and it can be seen that the average solid fraction in each of the simulations converges to this value after a sufficiently long time. For the convection simulations, it can be seen that the onset of convection results in much more rapid melting than for the case when only conduction is taking place. The step-like feature in the curves for the conduction case and for the case with $Ra/Ra_c = 2$ is a numerical artefact caused by the one-dimensional nature of the conduction solution. All of the grid points in a row melt completely at the same time. In figure 6(c), we present the average interface height as a function of time for the various simulations. We also include conduction-only calculations with values of ϵ of 0.1 and 100 for the sake of comparison. For the convection simulations, it can be seen that the interface begins to descend significantly only after the convective instability has set in. The amount by which the interface descends increases with the Rayleigh number of the simulation, as might be expected since vigorous convection will allow for efficient transport of solute away from the region of the interface. Even modest convection, as is the case for $Ra/Ra_c = 2$, results in significantly greater displacement of the interface than for a purely conductive simulation. However, even the largest Rayleigh-number simulation has the interface descend significantly less than the rapid-mixing theory of § 5 would predict. This indicates that some of the

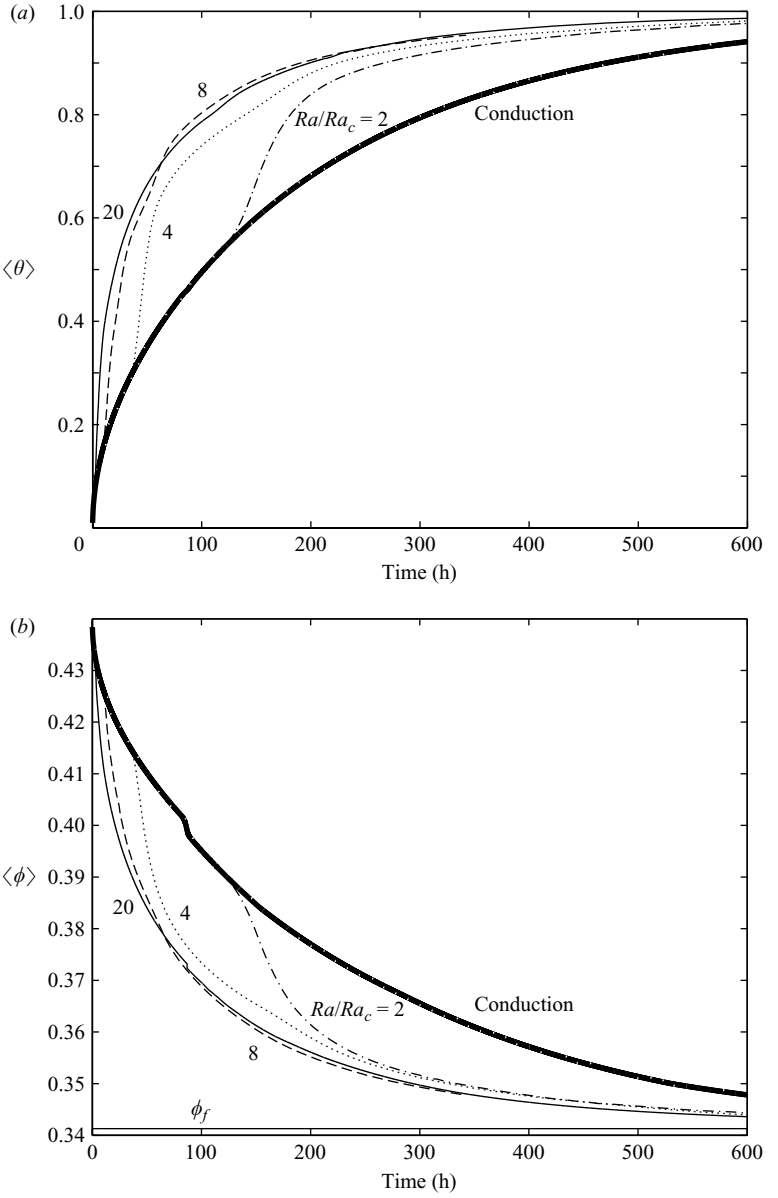

FIGURE 6(*a*, *b*). For caption see facing page.

heat from the surface boundary layer is penetrating into the interior of the mush even for this rapidly convecting case.

7. Results 2. The effects of varying the initial solid fraction

Figure 7 presents the results of a convection simulation with $Ra = 500$ with the same values of parameters as in table 1 except that the initial solid fraction has been decreased to 0.1. As we showed in § 5, this value is below the threshold for complete melting of the solid. The non-dimensional kinetic energy has been multiplied by 200 so as to be visible on this plot and hence its amplitude is not directly comparable to

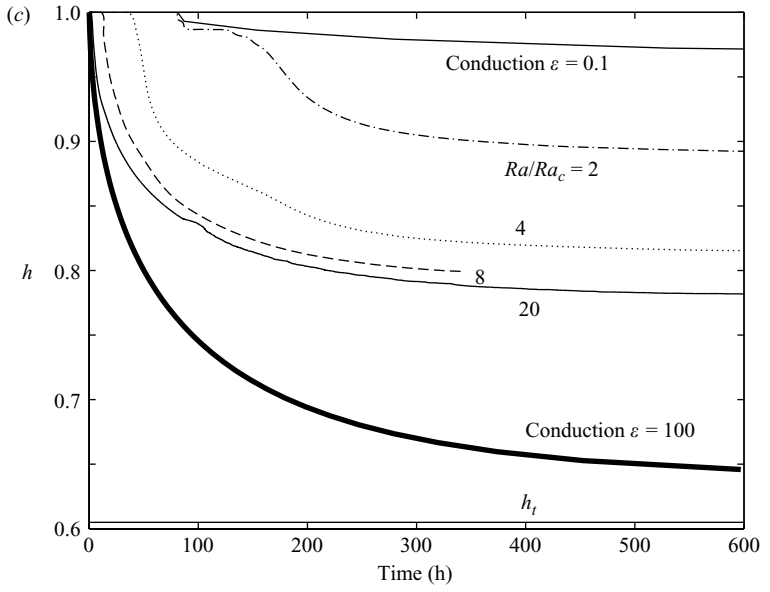

FIGURE 6. The evolution of volume-averaged quantities as a function of dimensional time for four simulations with different Rayleigh numbers (indicated on the figure) and one simulation in which the effects of convection have been suppressed. Ra_c has been estimated to be 125. (*a*) The non-dimensional volume-averaged temperature (*b*) the volume-averaged solid fraction and (*c*) the horizontally averaged non-dimensional interface height. (*c*) also displays the evolution of the height of the interface for a purely conductive calculation with $\epsilon = 100$.

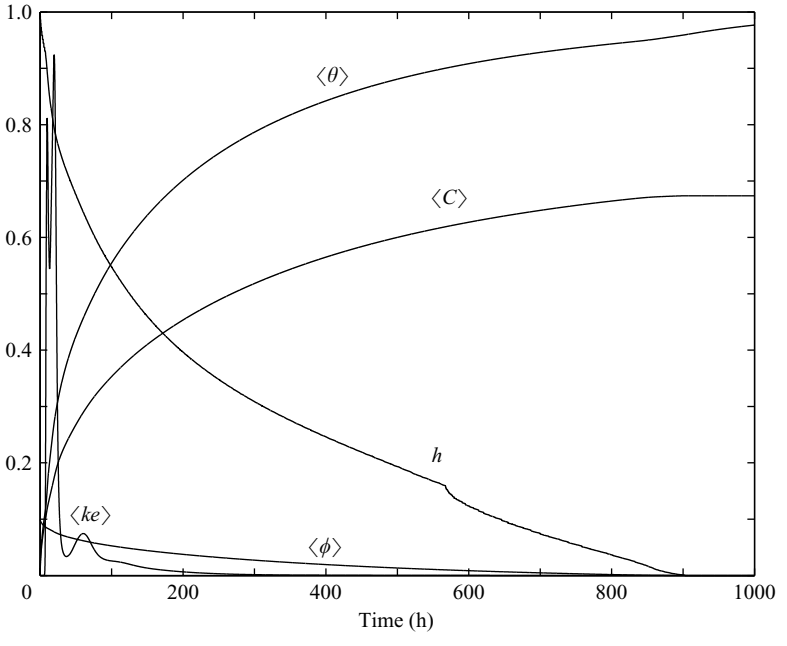

FIGURE 7. The volume-averaged temperature $\langle\theta\rangle$, concentration $\langle C\rangle$, solid fraction $\langle\phi\rangle$, and kinetic energy $\langle ke\rangle$ and the average interface height h, for a simulation with the same parameters as in table 1 except that the initial solid fraction is 0.1 and $Ra = 500$. The scaling of the kinetic energy is described in the text.

the calculations in figure 5. However, when scaled appropriately, the peak amplitude of the kinetic energy is 1.6 times higher for the $\phi_0 = 0.1$ case than for the $\phi_0 = 0.44$ calculation with $Ra = 500$ and the instability begins sooner for the low initial solid-fraction case and undergoes three transitions (as evidenced by the three bumps in the kinetic energy curve). This can be attributed to the higher permeability associated with the lower solid fraction which increases the effective Rayleigh number. The kinetic energy drops to 0 more quickly in the low initial solid-fraction case owing to the lower gravitational potential energy associated with a system with less total solute and is essentially 0 after 300 h. While the instability is taking place, the interface height drops rapidly. Unlike the simulations with a solid fraction of 0.44, the volume-averaged temperature and concentration are significantly different owing to the large melt region. After 300 h, the system evolves mostly by conduction and after roughly 900 h the mushy region has melted completely. After this time, the volume-averaged concentration field has a constant value of 0.67, which is close to the prediction of (5.4), and the temperature field slowly equilibrates with the upper boundary. The abrupt change in slope of the average interface height at 580 h occurs when the interface has descended to a height where there is a large region of low solid fraction within the mushy layer and the interface height subsequently drops very rapidly. The formation of lateral variations in the solid fraction within the mushy layer will be described in significantly more detail in § 9 in which we will examine a simulation with $\phi_0 = 0.44$ and $Ra = 2500$.

A further interesting regime may occur when ϕ_0 is large. As we indicated in § 5, ϕ_m may become greater than ϕ_0 and as a result, there may be regions in the mush where complete solidification takes place ($\phi = 1$). Our numerical model, in its current form, cannot handle the case of complete solidification. Some calculations were undertaken with $\phi_0 = 0.6$ at $Ra = 500$ (not shown). The main difference with the $\phi_0 = 0.44$ case was that convection was significantly less vigorous since the permeability was effectively decreased.

8. Results 3. The effects of varying the concentration ratio

In figure 8, we display the volume-averaged kinetic energy for the early stages of simulations using $Ra = 1000$. The values of $\mathscr{C}$ are indicated on the figure and the remainder of the parameter values are the same as those listed in table 1. The kinetic energy is in arbitrary units, but the same scaling is used for all of the simulations shown on the figure. As discussed in § 2, $\mathscr{C}$ determines the amount by which the concentration in the liquid changes for a given degree of solidification or melting, and the ratio $S/[\rho_s(C - \mathscr{C})]$ determines whether solute concentration or temperature is more strongly affected by a change in solid fraction. For the simulation calculated with $\mathscr{C} = 100$ corresponding to $S/[\rho_s \mathscr{C}] = 0.028$, there is little change in the solid fraction with the average value decreasing only slightly from 0.44 to 0.437 over the time to equilibration. Also, no melt region is formed and there is little spatial variability in the solid fraction field caused by convection. In this simulation, as heat diffuses in from the upper boundary, only a very small degree of melting is required to bring the solute concentration up to the liquidus value, the solute and heat transport are mostly governed by equation (2.1), and the system evolves in a similar manner to a thermally driven non-reactive porous medium with a negative thermal expansivity. The initial instability begins around time 20 h and consist of two rolls with a transition to a

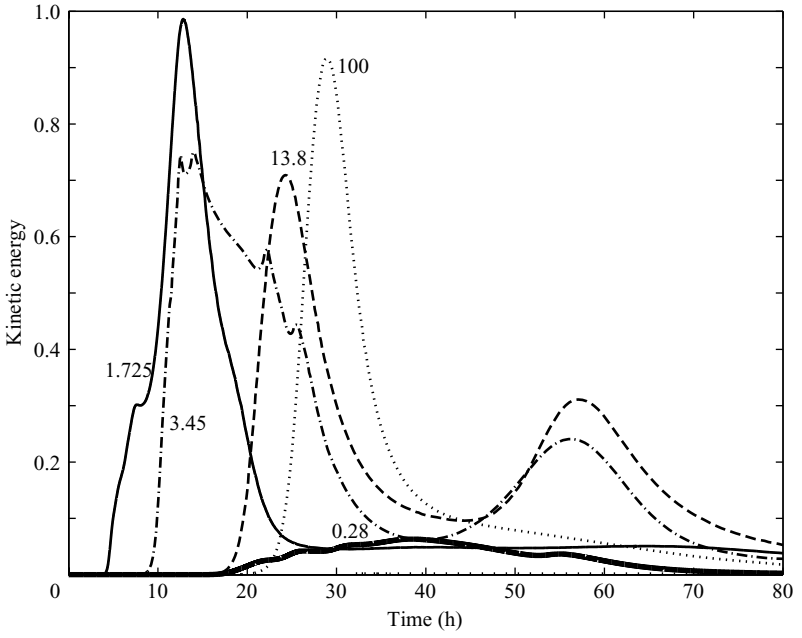

FIGURE 8. The kinetic energy as a function of time for simulations with the values of $\mathscr{C}$ indicated on the figure. All other parameters are those used in table 1.

very weak single-roll planform at time 120 h (not shown) as the buoyancy driving convection decreases.

The simulation with $\mathscr{C} = 13.8$ also does not form an upper melt region and the final average solid fraction was 0.42. Unlike the simulation with $\mathscr{C} = 100$, significant horizontal variations in the solid fraction field (not shown) were observed. The initial instability, corresponding to the peak at time 25 h in figure 8 consists of 3 rolls which switch to a single roll corresponding to the peak seen at time 58 h. The curve with $\mathscr{C} = 3.45$ is the same as the curve displayed in figure 5 with $Ra = 8Ra_c$. The initial instability in this simulation consists of 5 rolls with many subsequent changes in the convective planform which correspond to the various bumps seen on the kinetic energy curve. The final interface height for this simulation is 0.79 and the final volume-averaged solid fraction is 0.34. The final solid fractions mentioned above are all in excellent agreement with the predictions of equation (5.2). The initial instability for the calculation with $\mathscr{C} = 1.725$ corresponded to 7 rolls and the convective planform was also observed to change many times. This simulation was not run to equilibrium since a very large upper melt region was formed with $h_f < 0.5$ and the time for solute to diffuse into the melt region was excessively long. It can also be seen that the kinetic energy in this simulation becomes very weak at time 30 h which is due to the slow conductive transport of heat across the newly formed large melt region which is necessary for the release of buoyancy at the interface. In all of the simulations mentioned above, the interface was not observed to descend until the onset of convection. It can be seen that the time of onset for the initial instability increases with $\mathscr{C}$ and, as stated above, the number of convective rolls in the initial instability decreases. This is because the thermal and solute concentration fields in simulations with larger $\mathscr{C}$ evolve in a manner more similar to (2.1) than (2.2). Since

the thermal diffusivity, is much greater than the solute diffusivity, these simulations have a lower effective Rayleigh number and the onset of convection occurs when the thermal boundary layer from the surface has penetrated a greater distance into the domain. This can also be seen in equation (4.4) which shows that the critical Rayleigh number decreases with increasing $S/(\rho_s \mathscr{C})$. In the results of the simulations shown in figure 8, this effect is mitigated somewhat by the fact that in the early conductive stages of the calculation, the thermal boundary layer penetrates more rapidly into the domain when $\mathscr{C}$ is large. The tendency to more dramatic temporal changes in the convective planform with smaller values of $\mathscr{C}$ may in part be due to the convectively driven spatial variations in the solid fraction field and hence the permeability field. Examples of the spatial variation in the solid fraction field will be shown in the following section.

Also shown on the plot is the kinetic energy for a simulation with the very low value of $\mathscr{C} = 0.28$. This simulation was only run for a short time in order that $\mathscr{C}$ was always greater than C. In this case, a large melt region forms well before the onset of convection. As a result, melting at the interface is slow owing to the need for heat to diffuse across the large upper melt region and as a result, the convective instability is very weak.

The magnitude of $\mathscr{C}$ for a given system is determined by the concentration of solute in the solid phase, the slope of the liquidus, and the range of temperatures present in the system. For sea ice, using the data in Wettlaufer, Worster & Huppert (1997), a value of roughly $\mathscr{C} = 0.15$ is calculated, while for the experiments of Tait & Jaupart (1992) using ammonium chloride, $\mathscr{C}$ had the much larger value of 18.

9. Results 4. Largest Rayleigh number simulation

We present in figures 9(a) and 9(b) the liquid solute concentration and solid fraction fields 2.7 h into the simulation with $Ra = 2500$ with a Rayleigh number that is roughly 20 times the critical value. This time corresponds to an early stage of the instability at the surface. From the concentration field, it can be seen that only the right-hand side of the model domain has become unstable, owing to a small initial perturbation in the temperature and concentration fields, with many rolls of roughly unit aspect ratio. From the solid fraction field, it can be seen that the interface has only begun to descend appreciably where there is active convection taking place. It can also be seen that there are horizontal variations in the magnitude of the solid fraction. In the convection calculations, $\epsilon = 0.1$, as appropriate for thermal diffusion 10 times greater than solute diffusion. As a result, as a hot solute-rich downwelling fluid sinks, it equilibrates thermally with its surroundings more rapidly than it does compositionally. Also, a compositional front will propagate through a porous medium at the fluid velocity which can be related to the Darcy velocity as $u/(1-\phi)$ while temperature must equilibrate with the solid matrix and hence a temperature front will propagate at the slower rate of $u/\overline{\rho c_p}$ (Phillips 1991). Consequently, the solute front will propagate into the mushy layer faster than the temperature front. In order that the liquid stay on the liquidus, some of the solute must freeze onto the matrix, which results in a larger solid fraction in these regions. Cold solute-poor return flow to the surface must melt some of the solid for the same reasons. As a result, there are horizontal patterns of solid fraction that are above and below the initial solid fraction value of 0.44. It can also be seen that in regions of downwelling, the solid fraction is discontinuous across the interface while in regions of upwelling, the

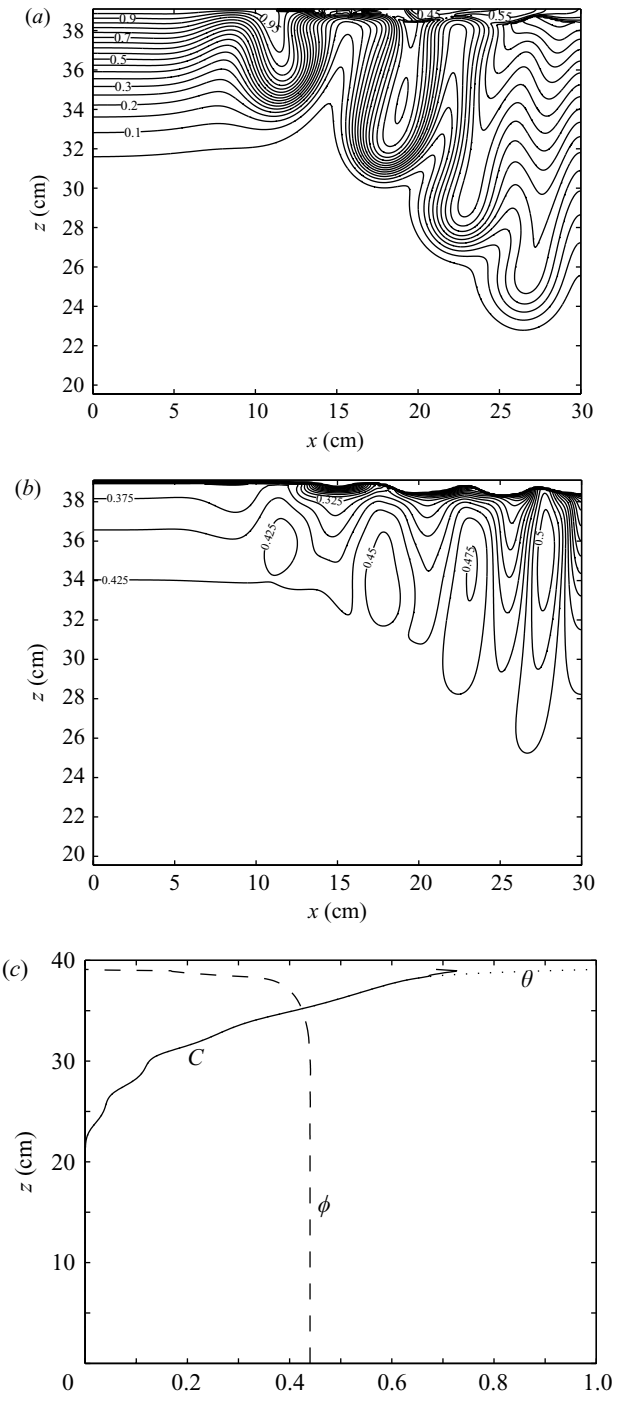

FIGURE 9. The liquid solute concentration C, solid fraction ϕ, and vertical profiles of horizontally averaged concentration, temperature and solid fraction are shown in (*a*), (*b*) and (*c*). The time is 2.7 h into the simulation and $Ra = 2500$. Only the top half of the solution domain has been plotted for the concentration and solid fraction as these fields are uniform in the lower half.

solid fraction goes continuously to 0 in accord with the theoretical model of Worster (2002). Complicating matters somewhat is the fact that the high and low patterns of the solid fraction reflect the history of convection through the mush and not only the current state of motion.

In figure 9(*c*), the horizontally averaged temperature, concentration and solid fraction are plotted as functions of height. Only in the top region where the interface has begun to descend are the temperature and concentration beginning to evolve separately. It can be seen that the high temperature and concentration, carried by the downwelling, have penetrated to just less than mid-depth of the tank.

In figure 10, we present contour plots of the concentration and solid fraction fields and plots of the horizontally averaged temperature, concentration and solid fraction at 6.1 h. A vector plot of the velocity field has been overlain on the contour plot of the concentration field in the figures. This time is just after the peak in kinetic energy and just as the dense down-going plume has penetrated to the bottom of the box. It can be seen that the system has now only two upwellings and two downwellings, a significant reduction from the situation at 2.7 h. The effects of the earlier, larger number of convection cells can be seen in the many highs and lows that remain in the solid fraction field near the surface. The temperature and concentration in the mush have been significantly increased by the penetration of the downwelling to the bottom of the tank, as can be clearly seen in figure 10*c*. This will result in a significant reduction in the buoyancy contrast between the material melted at the interface and the material in the interior of the mush which in turn results in significantly less vigour in subsequent flows. From the profiles, we can also see that a strong negative concentration gradient and positive temperature gradients have formed in the melt region. Both of these gradients are stabilizing and will result in relatively little fluid motion in the melt layer.

In figure 11, we plot vertical profiles of the horizontally averaged temperature, concentration and solid fraction at time 82.8 h, well after the initial spike in the kinetic energy. The height of the interface has descended to 34 cm and it can be seen that the interface is relatively sharp. The temperature and concentration in the mush have increased significantly and the concentration in the melt region has increased owing to diffusion. It is of interest that the temperature and concentration in the interior of the mush are not uniform as we might expect for a vigorously convecting system, but have a positive gradient. This feature persisted for most of the simulation, indicating that there was still a significant amount of heat carried by conduction into the mush. This is a further indication that a higher Rayleigh number would be necessary for the simple theory of § 5 to be applicable.

A contour plot of the solid fraction field once the volume-averaged temperature had reached 99 % of the surface value is plotted in figure 12(*a*) (time = 676 h). There remain two regions of high and low solid fraction corresponding to regions in which downwellings and upwellings had taken place in the past. The final convective instability consisted of a single roll after a transition from a two-roll pattern at 90 h. Convection at that point was very weak and had relatively little impact on the solid fraction field, however. The horizontally averaged temperature, concentration and solid fraction for this time are presented in figure 12(*b*). It can be seen that the temperature and concentration have essentially equilibrated with the surface temperature. The solid fraction in the mush has not changed significantly from its initial value, indicating that the effects of melting from heat conducted into the mush, which will tend to decrease the solid fraction, have essentially nullified the effects

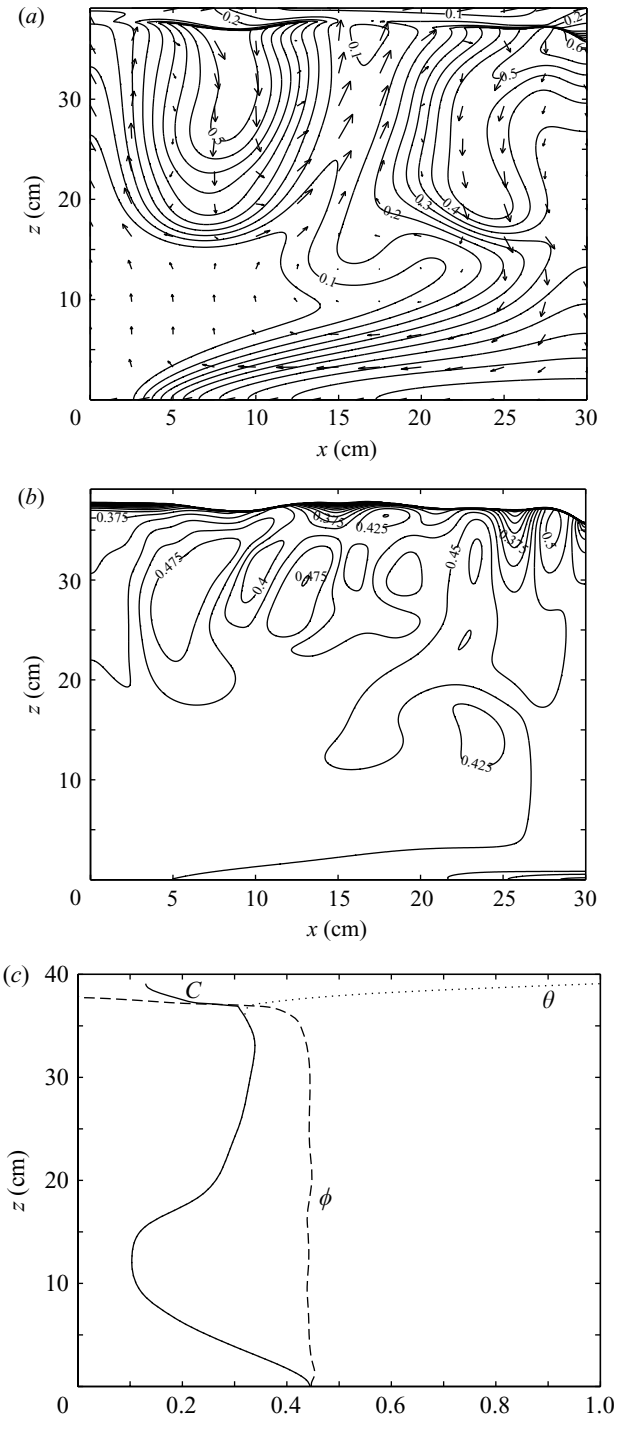

FIGURE 10. The liquid solute concentration C, with an overlain vector plot of the fluid velocity, solid fraction, ϕ, and vertical profiles of horizontally averaged concentration, temperature and solid fraction are shown in (*a*), (*b*) and (*c*). The time is 6.1 h and $Ra = 2500$. A warm downwelling has just penetrated into the lower layer.

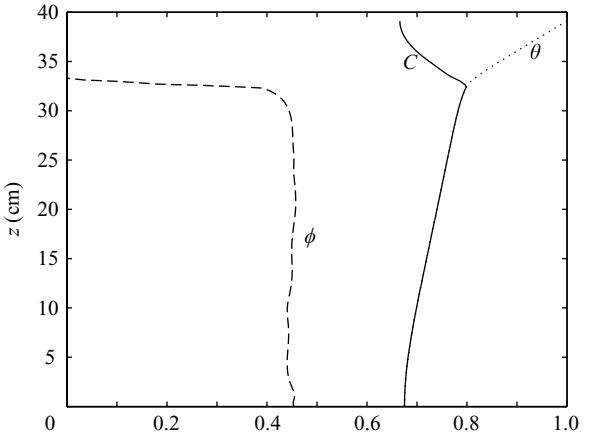

FIGURE 11. Vertical profiles of the horizontally averaged non-dimensional temperature θ, concentration C and solid fraction ϕ at 82.8 h.

due to rapid transport of solute into the mush, which will tend to increase the solid fraction. The solid fraction in the mush is significantly less than the ϕ_m predicted from the theory presented in § 5, and the interface has descended significantly less than this theory would predict because a significant amount of conductive heat from the surface has penetrated into the bulk of the mushy layer. It should be mentioned that in real experimental and geological systems, the time for solute to diffuse into the melt region would be significantly increased since solute diffusivity would be roughly one order of magnitude smaller. For a magma chamber where the melt region was 10 m deep, where a typical solute diffusivity is 10^{-9} m^2 s^{-1}, it would take roughly 3000 years. It is likely that the surface temperature would have changed in that time.

In figure 12(c) we plot the non-dimensional mass concentration of solute in the liquid and solid and the total solute mass concentration as a function of depth for time 676 h. Also indicated is the initial value of this quantity that was uniform everywhere. It can be seen that most of the solute in the mush resides in the solid while there has been a significant transfer of solute from the melt to the mush region during the course of the calculation. As a check on the numerical calculation, the total solute concentration changed by only 1.3 % during the course of the calculation.

10. Comparison of numerical and laboratory experiments

One advantage of the numerical experiment is that it was possible to run the simulation to equilibrium whereas the heating from the laboratory became a factor in the experimental investigation after roughly 24 h. Because of this, we were able to compare the final state of the numerical model with the final state predictions of the simple theory. It was found that even for the highest Rayleigh-number simulations, the system was not in a regime in which solute was removed effectively instantaneously from the interface region and as a result, the interface did not descend to the extent predicted by the simple theory. Although the laboratory experiment could not be run to equilibration owing to the eventual effects of heating from the laboratory, the evolution of the interface agreed well with the simple theory presented by Hallworth *et al.* (2004), indicating that the experiment took place under conditions in which solute was removed effectively instantaneously from the interface region (the infinite-Rayleigh-number limit). Other indications that the experiment was undertaken at a

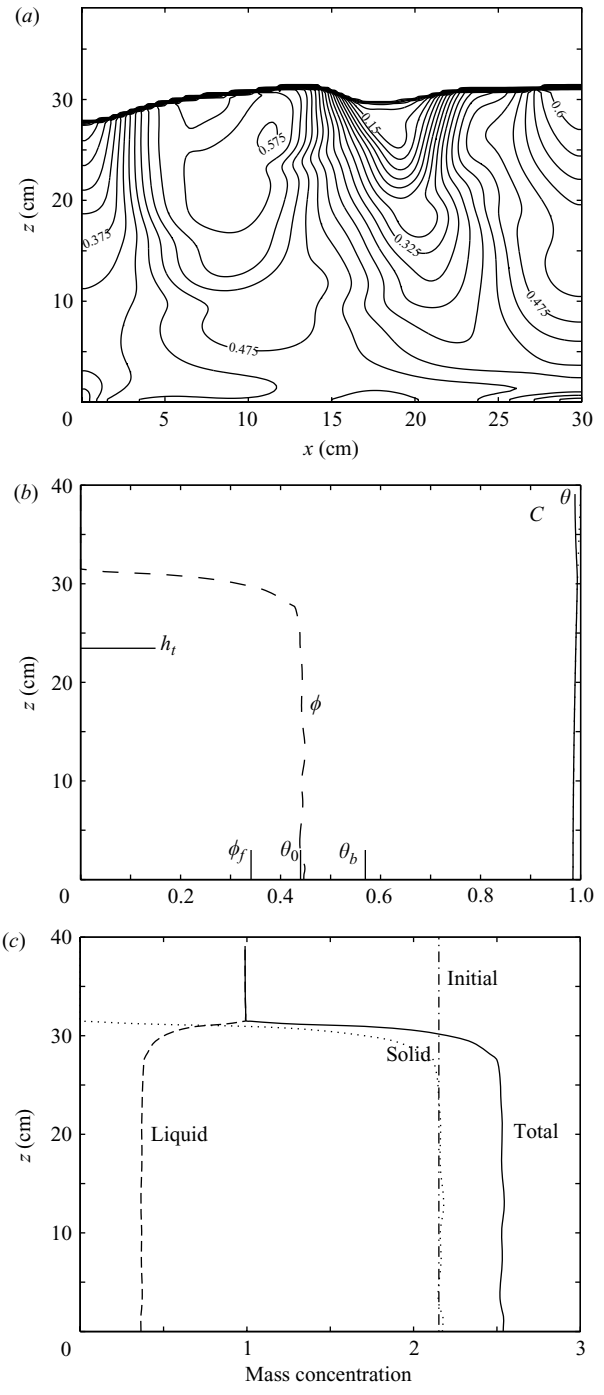

FIGURE 12. A contour plot of the solid fraction field ϕ, vertical profiles of the horizontally averaged temperature θ, concentration C and solid fraction as well as vertical profiles of the horizontally averaged non-dimensional solute concentration in the liquid, solid and total concentration are shown in (*a*), (*b*) and (*c*). The time is 676 h (once the average temperature of the system was 99 % of the surface temperature). Also indicated in (*b*) are the predicted final height h_t and bulk solid fraction ϕ_b from the theory of § 5 as well as the initial solid fraction ϕ_0 and the predicted average solid fraction ϕ_f. Also indicated in (*c*) is the initial value of the total concentration that was uniform with depth.

higher Rayleigh number than the simulations include the fact that convection was seen to initiate almost instantly when the upper surface temperature was increased in the experiment, whereas in the simulations there was a purely conductive stage until the surface thermal boundary layer had achieved a critical thickness. This critical thickness decreased with the Rayleigh number. The interface was seen to descend significantly more rapidly in the experiment than in the numerical simulation as also did the increase in the internal temperature. Based on the short time required for convection to begin in the experiment, we estimate its Rayleigh number to be at least 15 000. A direct calculation of the Rayleigh number characterizing the experiments, based on the properties of the system, yields a large range of values owing to the large uncertainty in the permeability of the porous medium. A Rayleigh number of 15 000 would require a permeability of roughly $4 \times 10^{-10}\,\mathrm{m}^2$ which is a reasonable value for a coarsely packed system. Boundary layers decrease linearly with increasing Rayleigh number for low Rayleigh numbers (Elder 1967; Vadasz 2001) for porous-medium convection implying a need to increase the resolution of the simulation rapidly as the Rayleigh number increases. A resolution increase by the amount necessary is beyond our current computational capabilities. The implementation of a non-uniform numerical grid with higher resolution in the vicinity of the interface where short length-scale solute variations take place might also make higher-Rayleigh-number calculations feasible.

A further difference between the laboratory experiments and the simulations is that the former were inherently three-dimensional whereas the latter were two-dimensional, and hence it was assumed that there were no variations in any of the variables characterizing the system in the third space dimension. This latter case is physically the same as if the confining walls of the tank were closely spaced so as not to allow any flow in the third dimension and free-slip, whereas in the experiment they were 2 cm apart and no-slip. Hence, one effect of the sidewalls in the experiment was to induce drag on the flow that was not present in the simulations. Despite this added source of drag, convection in the experiments was significantly more vigorous than in the simulations due to the higher Rayleigh number. Flow in the experiments was observed to be dominantly two-dimensional, which is consistent with the results of the simulations since only at the onset of convection would any of the convective rolls have a horizontal wavelength less than 2 cm (when the vertical length is scaled by 39 cm).

11. Discussion and conclusions

We have presented a numerical model of convection in a reactive porous medium. The model has been used to investigate the instability that occurs owing to dissolution of a reactive porous medium when heated from above and the degree of melting that takes place at the interface and within the mush. We have demonstrated that for the parameters used here, the critical Rayleigh number for the onset of convection lies between 100 and 175. The amount by which the interface descends has been shown, in the conduction calculation reported herein, to be a function of the efficiency with which solute can be removed from the region of the interface, with a maximum displacement occurring when all of the heat from the surface was taken up in melting the interface region. Similarly, the interface displacement increases with increasing Rayleigh number. The largest-Rayleigh-number calculations still show displacements that are significantly less than the limit at which all of the heat from the surface is

used to cause melting at the interface. The largest-Rayleigh-number simulations are also still at significantly lower Rayleigh number than the analogue we experiments of Hallworth *et al.* (2004).

The final state of the system consists of an upper melt region and a lower mush region with significant topography on the boundary between these regions. The solid fraction within the mush region is greater than its initial value in regions where downward flow was taking place and was decreased in regions where upward flow was taking place. The solid fraction goes continuously to zero at the interface in regions of upward flow and drops discontinuously in regions of downward flow. The pattern of solid fraction in the final state also reflects earlier flow patterns; and the flow pattern was seen to rearrange itself a number of times during the simulation. Understanding the factors affecting the final arrangement of the solid fraction may help understand textures and layering seen in igneous rock formations.

This paper was partially completed while H. E. H. was a Gledden Fellow at the University of Western Australia. He thanks Jörg Imberger and the other members of the Centre for Water Resources for their kind hospitality during his visit. We are also grateful to Peter Guba for his helpful comments on an early draft of the paper.

Appendix. Numerical scheme

The full forms of the quantities Θ_1, Θ_2, CON_1 and CON_2 used in equations (4.1) and (4.2) are

$$\Theta_1 = \left\{\theta_{i,j}^{n-1/2}\left\{1 - \frac{\Delta t\bar{k}}{Ra\overline{\rho c_p}}\left(\frac{1}{\Delta x^2} + \frac{1}{\Delta z^2}\right)\right\} + \Delta t\left\{-J(\psi,\theta)\right.\right.$$
$$+ \frac{\bar{k}}{Ra}\left[\frac{\theta_{i+1,j}^n + \theta_{i-1,j}^n}{\Delta x^2} + \frac{\theta_{i,j+1}^n + \theta_{i,j-1}^n}{\Delta z^2}\right] + \frac{k_s - 1}{Ra}\left[\frac{\left(\phi_{i+1,j}^n - \phi_{i-1,j}^n\right)\left(\theta_{i+1,j}^n - \theta_{i-1,j}^n\right)}{4\Delta x^2}\right.$$
$$\left.\left.\left. + \frac{\left(\phi_{i,j+1}^n - \phi_{i,j-1}^n\right)\left(\theta_{i,j+1}^n - \theta_{i,j-1}^n\right)}{4\Delta z^2}\right]\right\}\right\} \Big/ \left\{\overline{\rho c_p}\left(1 + \frac{\Delta t\bar{k}}{Ra\overline{\rho c_p}}\left(\frac{1}{\Delta x^2} + \frac{1}{\Delta z^2}\right)\right)\right\}, \tag{A 1}$$

$$\Theta_2 = 2S \Big/ \left[\overline{\rho c_p} + \frac{\Delta t\bar{k}}{Ra}\left(\frac{1}{\Delta x^2} + \frac{1}{\Delta z^2}\right)\right], \tag{A 2}$$

$$CON_1 = \left\{C_{i,j}^{n-1/2}\left\{1 - \frac{\Delta t\epsilon}{Ra}\left(\frac{1}{\Delta x^2} + \frac{1}{\Delta z^2}\right)\right\} + \Delta t\left\{-J(\psi, C)/\left(1 - \phi_{i,j}^n\right)\right.\right.$$
$$+ \frac{\epsilon}{Ra}\left[\frac{C_{i+1,j}^n + C_{i-1,j}^n}{\Delta x^2} + \frac{C_{i,j+1}^n + C_{i,j-1}^n}{\Delta z^2}\right]$$
$$- \frac{\epsilon}{(1 - \phi_{i,j}^n)Ra}\left[\frac{\left(\phi_{i+1,j}^n - \phi_{i-1,j}^n\right)\left(C_{i+1,j}^n - C_{i-1,j}^n\right)}{4\Delta x^2},\right.$$
$$\left.\left.\left. + \frac{\left(\phi_{i,j+1}^n - \phi_{i,j-1}^n\right)\left(C_{i,j+1}^n - C_{i,j-1}^n\right)}{4\Delta z^2}\right]\right\}\right\} \Big/ \left\{\left(1 + \frac{\Delta t\epsilon}{Ra}\left(\frac{1}{\Delta x^2} + \frac{1}{\Delta z^2}\right)\right)\right\}, \tag{A 3}$$

$$CON_2 = 2\rho_s\left(C^n_{i,j} - \mathscr{C}\right) \Big/ \left[\left(1-\phi^n_{i,j}\right)\left(1+\frac{\Delta t\epsilon}{Ra}\left(\frac{1}{\Delta x^2}+\frac{1}{\Delta z^2}\right)\right)\right]. \qquad (A\,4)$$

The operator J represents the Arakawa Jacobean.

REFERENCES

Adams, J. 1991 Recent enhancement in MUDPACK, a multigrid software package for elliptic partial differential equations. *Appl. Maths Comput.* **43**, 79–93.

Arakawa, A 1966 Computational design for long-term numerical integration of the equations of fluid motion: two-dimensional incompressible, Part 1. *J. Comput. Phys.* **1**, 119–143.

Beckermann, C. & Wang, C. Y. 1995 Transport phenomenon in alloy solidification. In *Annual Review of Heat Transfer VI* (ed. C. L. Tien), pp. 115–198. Begell House.

Carmen, P. C. 1939, Permeability of saturated sands soils and clays. *J. Agric. Sci.* **29**, 262–273.

Chiareli, A. O. P., Huppert, H. E. & Worster, M. G. 1994 Segregation and flow during the solidification of alloys. *J. Cryst. Growth* **139**, 134–146.

Crank, J. 1984 *Free and Moving Boundary Problems*. Clarendon.

Elder, J. W. 1967 Steady free convcection in a porous medium heated from below. *J. Fluid Mech.* **27**, 29–48.

Feltham, D. & Worster, M. G. 2000 Similarity solutions describing the melting of a mushy layer. *J. Cryst. Growth* **208**, 746–756.

Hallworth, M., Huppert, H. E. & Woods, A. W. 2004 Disolution driven convection in a reactive porous medium. *J. Fluid Mech.* **535**, 255–285.

Huppert, H. E. 1990 The fluid mechanics of solidification. *J. Fluid Mech.* **212**, 209–240.

Huppert, H. E. 2000 Geological fluid mechanics. In *Perspectives in Fluid Dynamics* (ed. G. K. Batchelor, H. K. Moffatt, & M. G. Worster), pp. 447–506. Cambridge University Press.

Huppert, H. E. & Turner, J. S. 1981 A laboratory model of a replenished magma chamber. *Earth Plant. Sci. Lett.* **54**, 144–152.

Irvine, T. N. 1982 Terminology for layered intrusions. *J. Petrol.* **23**, 127–162.

Jaupart, C. & Tait, S. 1995 Dynamics of differentiation in magma reservoirs. *J. Geophys. Res.* **100**, 17 615–17 636.

Kerr, R. C. 1994*a* Melting driven by vigorous compositional convection. *J. Fluid. Mech.* **280**, 255–285.

Kerr, R. C. 1994*b* Dissolving driven by vigorous compositional convection. *J. Fluid. Mech.* **280**, 287–301.

Kerr, R. C. & Tait, S. 1986 Crystallization and compositional convection in a porous medium cooled from below with application to layered igneous intrusions. *J. Geophys. Res.* **91**, 3591–3608.

Martys, N. S., Torquato, S. & Bentz, D. P. 1994 Universal scaling of fluid permeability for sphere packing. *Phys. Rev.* E **50**, 403–408.

Phillips, O. M. 1991 *Flows and Reactions in Permeable Rocks*. Cambridge University Press.

Saar, M. O. & Manga, M. 2002 Continuum percolation for randomly oriented soft-core prisms. *Phys. Rev.* E **50**, 056131.

Shyy, W., Udaykumar, H. S., Rao, M. M. & Smith, R. W. 1995 *Computational Fluid Dynamics with Moving Boundaries, Series in Computational and Physical Processes in Mechanics and Thermal Sciences*. Taylor & Francis.

Tait, S. & Jaupart, C. 1992 Compositional convection in a reactive crystalline mush and melt differentiation. *J. Geophys. Res.* **97**, 6735–6756.

Turner, J. S. & Gustafson, L. B. 1978 The flow of hot saline solutions from vents in the sea floor – some implications for exhalative massive sulfide and other ore deposits. *Econ. Geol.* **73**, 1082–1100.

Vadasz, P. 2001 Heat transfer regimes and hysteresis in porous media convection. *J. Heat Transfer* **123**, 145–156.

Wager, L. R. & Brown, G. M. 1968 *Layered Igneous Rocks*. Oliver & Boyd.

Wettlaufer, J. S., Worster, M. G. & Huppert, H. E. 1997 Natural convection during solidification of an alloy from above with application to the evolution of sea ice. *J. Fluid. Mech.* **344**, 291–316.

Worster, M. G. 1992 The dynamics of mushy layers. In *Interactive Dynamics of Convection of Solidification* (ed. S. H. Davis, H. E. Huppert, W. Müller & M. G. Worster), pp. 113–138. Kluwer.

Worster, M. G. 2000 Solidification of fluids. In *Perspectives in Fluid Dynamics* (ed. G. K. Batchelor, H. K. Moffatt & M. G. Worster), pp. 393–446, Cambridge University Press.

Worster, M. G. 2002 Interfaces on all scales during solidification and melting (ed. K. Smith, M. Miksis, G. McFadden, G. P. Neitzel & D. Canright), pp. 187–201. Imperial College Press.